Oxygen-vacancy and phosphorus-doping enriched NiMoO4 nanoarrays for high-energy supercapacitors

Oxygen-vacancy and phosphorus-doping enriched NiMoO4 nanoarrays for high-energy supercapacitors

Zhengju Zhu[a], Ling Zang[b], Mingshan Chu[a], Ying Hea, Dayong Ren[c,*], Petr Saha[d], Qilin Cheng[a,d,]**

[a]*Key Laboratory for Ultrafine Materials of Ministry of Education, Shanghai Engineering Research Center of Hierarchical Nanomaterials, School of Materials Science and Engineering, East China University of Science and Technology, Shanghai 200237, China*

[b]*School of Resources and Environmental Engineering, East China University of Science and Technology, Shanghai 200237, China*

[c]*State Key Laboratory of High Performance Ceramics and Superfine Microstructure, Shanghai Institute of Ceramics, Chinese Academy of Sciences, Shanghai 200050, China*

[d]*Sino-EU Joint Laboratory of New Energy Materials and Devices, Tomas Bata University in Zlin, nam. T. G. Masaryka 5555, 760 01 Zlin, Czech Republic*

**Corresponding author:*

***Correspondence to: Q. Cheng, Key Laboratory for Ultrafine Materials of Ministry of Education, Shanghai Engineering Research Center of Hierarchical Nanomaterials, School of Materials Science and Engineering, East China University of Science and Technology, Shanghai 200237, China. E-mail addresses: rendayong@mail.sic.ac.cn (D. Ren), chengql@ecust.edu.cn (Q. Cheng).*

ABSTRACT

Exploring electrode materials with high effective surface and abundant active sites takes on a critical significance in achieving high-energy supercapacitors. Herein, the oxygen vacancies (O_v) and P-doping enriched $NiMoO_4$ nanosheet arrays were synthesized through the combination of phosphorization and N_2 plasma treatment. The combination strategy makes it possible to sharply increase and modulate the O_v content. The optimized P-$NiMoO_4$-N_2 is found with the highest O_v content, and the capacitive activity is well consistent with the increase in the O_v content among all samples. As revealed by experimental results, rich O_v increases the electrochemically accessible active-sites while enhancing the intrinsic conductivity. Thus, the optimized P-$NiMoO_4$-N_2 is enabled to reach a high capacity of 2180 F g^{-1} at a current density of 1 A g^{-1} and remains 83.9 % at 10 A g^{-1} with high cycling stability. After being assembled with activated carbon as the negative electrode, the asymmetric supercapacitor exhibits a high energy density of 56.8 Wh kg^{-1} at 0.75 kW kg^{-1} and maintains 41.6 Wh kg^{-1} at 15 kW kg^{-1}. This work may create a novel path to enrich and adjust Ov in metal oxides for high-capacity and high-power supercapacitors.

Keywords: Oxygen vacancy, $NiMoO_4$, phosphorus doping, N_2 plasma, supercapacitor

1. Introduction

Supercapacitors have been generally accepted as one of the most essential energy storage devices for the application of renewable energy sources. In accordance with the energy storage mechanism,

supercapacitors can fall into two types, including, electric double layer capacitances (EDLCs) via adsorption/desorption of electrolyte ions on/ from the electrode surface and pseudocapacitors through the fast reversible faradaic reactions [**1,2**]. In general, EDLCs exhibit the advantage of ultrahigh power density and excellent stability, while pseudocapacitors are capable of leading to a higher energy density. Developing electrode materials with high capacity is of great urgency and significance in further increasing the energy density of supercapacitor [**3,4**]. A wide variety of electrode materials involving advanced carbon materials with doped heteroatoms as redox-active sites [**5,6**], electroactive porphyrin polymers [**7**], metal oxides [**8**], metal hydroxides [**9,10**], and metal phosphides [**11**] have been investigated in terms of high-performance supercapacitors. Among a range of metal oxides, binary transition metal oxides have recognized as promising candidates for their superior specific capacitance and synergistic effect between binary metal ions [**8,12**]. For example, $NiMoO_4$ has aroused wide attentions for its abundance, strong chemical stability, as well as high theoretical capacity [**13-16**]. However, $NiMoO_4$ is subjected to intrinsic problems (e.g., low electrical conductivity, sparse active sites, and large volume changes during cycling), thus hindering the practical application of $NiMoO_4$ [**17**].

To solve the above problems of $NiMoO_4$, great endeavors have been taken to construct proper nanostructures with a high specific surface area and abundant pore structures, thus increasing the electrode/elec-trolyte contact area and the ion diffusion rate, while exposing more electrochemical active sites to increase the capacity [**18-20**]. However, the morphological design does not enhance the intrinsic properties of $NiMoO_4$, making it difficult to further increase the capacity. First principle calculations have demonstrated that defect engineering is capable of building atomic level defects (e.g. oxygen vacancy) on metal oxides, resulting in lattice distortions and the regulation of electron structure, which can increase the intrinsic activity, conductivity and active sites number [**21**]. For example, Wang et al. creates oxygen vacancies (O_v) in the $NiMoO_4$ nanosheets using a P-doping strategy [**22**]. Minakshi et al. have combined theoretical and experimental methods to confirm that the appropriate amount of Zn dopant in $NiMoO_4$ could increase the storage capacity due to O_v interactions [**12**]. The as-prepared electrode with significantly increased intrinsic activity and wettability exhibits a high area specific capacity. Although O_v-enriched $NiMoO_4$ has been proven to be more efficient than the counterpart without O_v, the tunability of O_v amounts in $NiMoO_4$ and the effect arising from the concentration of O_v in $NiMoO_4$ on the supercapacitor performances have been rarely investigated. Thus, the correlation of energy storage performances of $NiMoO_4$ with the concentration of O_v remains unclear, and the development of a feasible preparation strategy to modulate amounts of O_v is still difficult task.

In this work, to increase the intrinsic conductivity of $NiMoO_4$ and further develop high-performance $NiMoO_4$ supercapacitors, a facile phosphorization and subsequent N_2 plasma treatment were experimentally established to dramatically increase the content of O_v and provide insight into how the content of O_v affects the electrochemical performances of $NiMoO_4$. A self-supported electrode of O_v-rich $NiMnO_4$ nanosheets arrays (P-$NiMoO_4$-N_2) on cobalt (Co) foam was obtained based on the developed strategy. It is found that the electrochemical performance of P-$NiMoO_4$-N_2 is in accordance with the increase of the concentration of Ov, which is superior to that of its counterparts with fewer O_v. As a result, a high specific capacitance of 2180 F g^{-1} at 1 A g^{-1} was achieved and maintained 83.9 % at 10 A g^{-1} with high cycling stability of P-$NiMoO_4$-N_2. The experimental results verify that the high concentration of O_v accounts for the improvement of inherent conductivity and increase of active sites number in $NiMnO_4$. Moreover, the simultaneous P doping and the nanosheet morphology facilitate the surface wettability and electrolyte permeation, leading to the high utilization of active materials.

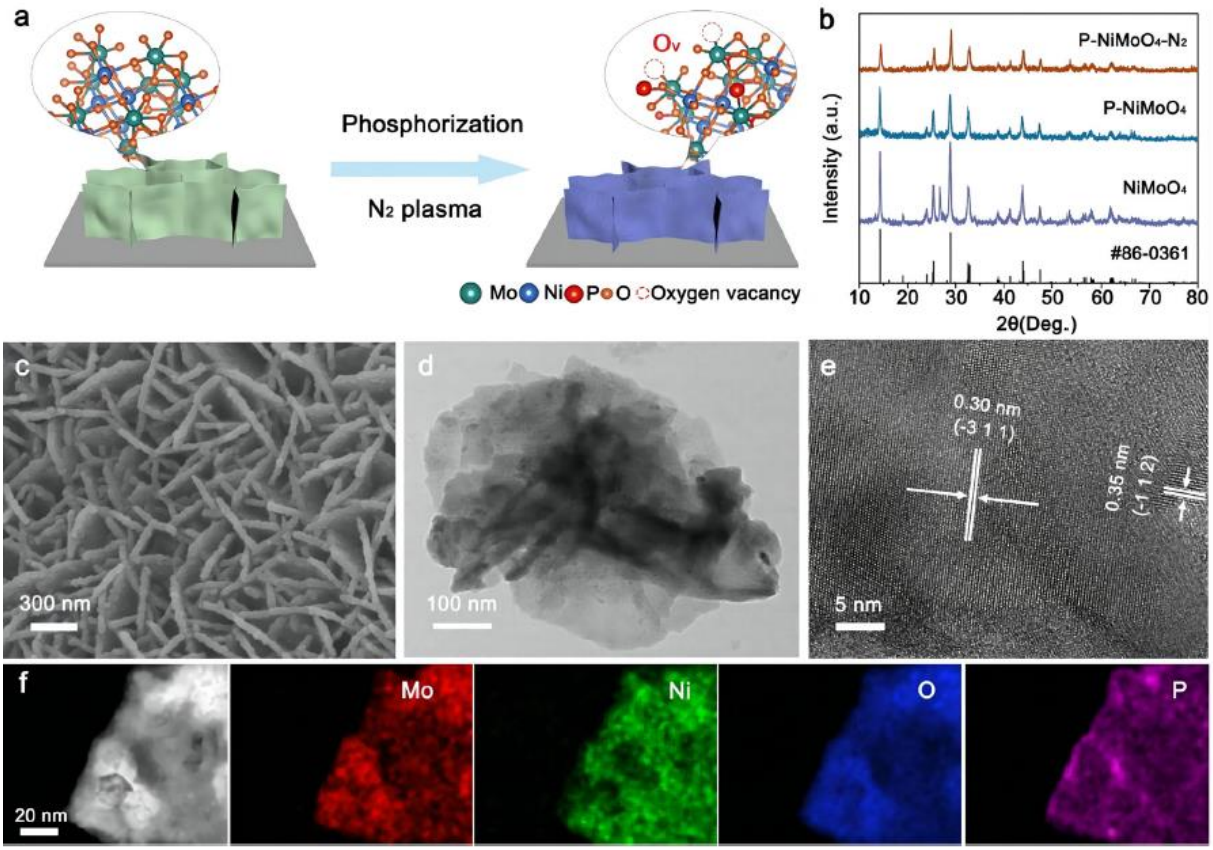

Fig. 1. (a) Schematic illustration of the preparation process of the P-$NiMoO_4$-N_2 nanosheets arrays, (b) XRD patterns of $NiMoO_4$, P-$NiMoO_4$ and P-$NiMoO_4$-N_2, (c) SEM image, (d) TEM image, (e) HRTEM image and (f) TEM-EDS mapping of P-$NiMoO_4$-N_2.

An asymmetric supercapacitor (ASC) with as-prepared P-$NiMoO_4$-N_2 as the positive electrode and activated carbon as the negative electrode was well constructed. The optimal ASC delivers a high energy density of 56.8 Wh kg^{-1} at 0.75 kW kg^{-1}, which was maintained as 41.6 Wh kg^{-1} at 15 kW kg^{-1}. The findings provide a promising strategy to adjust and maximize the Ov content in the metal oxide electrode for developing efficient supercapacitors and other relevant electrochemical applications.

2. Experimental

2.1. Material synthesis

Synthesis of $NiMoO_4$ nanosheet arrays: 0.291 g of $Ni(NO_3)_2$-$6H_2O$ and 0.242 g of Na_2MoO_4-$2H_2O$ were mixed in a solution composed of 15 ml water and 15 ml ethanol. After that, the above solution and one acid-treated cobalt foam (2 cm x 3 cm x 0.3 mm) were added into a 50 ml Teflon-lined stainless autoclave and then heated at 160 °C for 6 h. The choice of Co foam rather than nickel (Ni) foam is to avoid the effect of Ni metal inside Ni foam on the characterization of Ni elements in $NiMoO_4$. The processed Co foam was taken out from the solution, washed and dried. Finally, the precursor was heated to 450 ° C at 1 ° C min^{-1} for 2 h in the inert gas. The active material weight of the $NiMoO_4$ on Co foam was found to be 0.5 mg cm^{-2}.

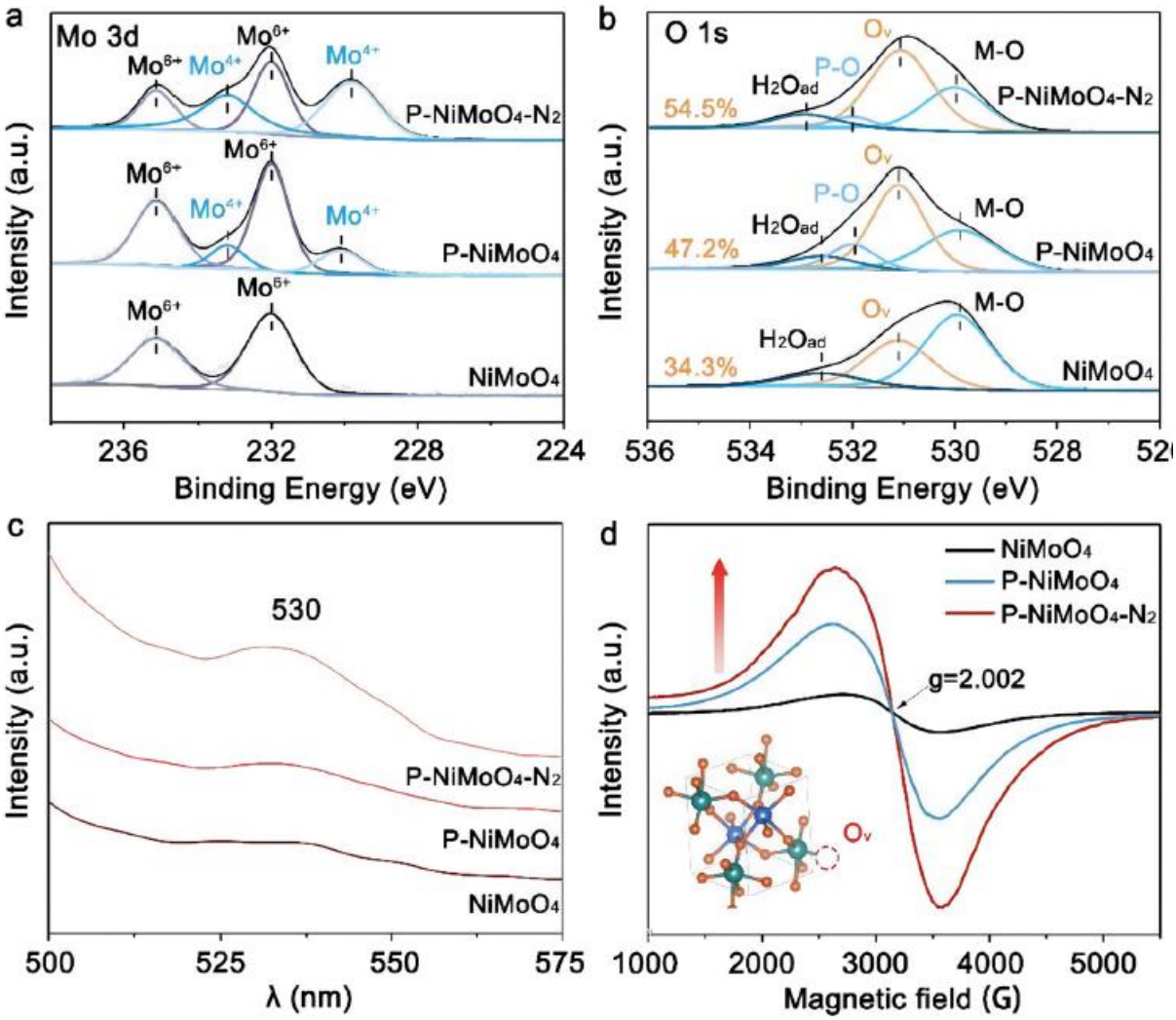

Fig. 2. High-resolution XPS spectra of (a) Mo 3d, (b) O 1s, (c) Photoluminescence (PL) spectra and (d) EPR spectra (inset shows schematic illustration of oxygen vacancy) of $NiMoO_4$, P-$NiMoO_4$ and P-$NiMoO_4$-N_2.

Preparation of P-$NiMoO_4$ electrode: 0.5 g of NaH_2PO_2 and as-prepared $NiMoO_4$ nanosheet arrays were put in separate positions in a porcelain boat with NaH_2PO_2 at the upstream side of the furnace. When the porcelain boat was heated to 300 ° C for 2 h under the Ar atmosphere, NaH_2PO_2 decomposed into $Na_4P_2O_7$ and PH_3. Then, the PH_3 gas reacted with as-prepared $NiMoO_4$ electrode to form P-$NiMoO_4$ electrode.

Preparation of P-$NiMoO_4$-N_2 electrode: The as-prepared P-$NiMoO_4$ electrode was placed in the N_2 atmosphere and heated up to 450 °C. During N_2 plasma treatment, the N_2 pressure is kept at 60 Pa and reacted with 250 W plasma source for 10 min to obtain P-$NiMoO_4$-N_2.

2.2. Material characterization

X-ray powder diffraction (XRD, Bruker D8 Advance, Cu Ka radiation), field emission scanning electron microscopy (FESEM, Hitachi, S-4800) and transmission electron microscopy (TEM; JEOL, JEM-2100F) with an X-ray energy dispersive spectrometer (EDS) at an accelerating voltage of 200 kV were employed to characterize morphology and structure of as-obtained products. For XRD samples, P-$NiMoO_4$-N_2, P-$NiMoO_4$, and $NiMoO_4$ nanosheets arrays exfoliated from Co foams under the sonication

were used. The surface characterizations were determined by the X-ray photoelectron spectroscopy spectra (XPS, AXIS Ultra DLD spectrometer, Al Ka X-ray radiation), photoluminescence spectra (PL, PE, LS-55) and electron paramagnetic resonance spectra (EPR, Bruker, EMX-8/2.7).

2.3. Electrochemical measurements

Electrochemical characterizations were carried out in 1 M KOH solution by a standard three-electrode system with as-prepared electrodes serving as the working electrode, the platinum foil counter electrode and saturated calomel electrode (SCE) reference electrode. All electrochemical experiments were tested and recorded on Autolab PGSTAT302N. Specific capacitance was calculated from the equation: $C_s = (I \text{ x } \Delta t) \text{ / } (V \text{ x } m)$ according to GCD curves, where I represents the applied current, Δt means the discharge time, m is the mass of the active material within the active area, and V is the voltage window. The impedance spectra were recorded at 0 V vs. SCE reference electrode from 0.01 Hz to 100 kHz.

The asymmetric supercapacitor (ASC) was assembled from P-$NiMoO_4$_N_2 positive electrode and activated carbon (AC) negative electrode, which is denoted as P-$NiMoO_4$_ N_2//AC. Especially, AC was mixed with carbon black (Super P) and polyvinylidene fluoride (PVDF) following the mass ratio of 8:1:1 to obtain a slurry, and then coated on carbon paper to obtain the negative electrode. The prepared P-$NiMoO_4$_N_2 was separated from the activated carbon with non-woven fabrics (NKK), supplemented with gaskets, shrapnel, positive and negative cell shells, then dripped with 1 M KOH as the electrolyte, and finally assembled into a button-type device to form the asymmetric device. The energy density (E) of the asymmetric supercapacitor was calculated from the equation: $E = (C_s \text{ x } V^2) \text{ / } (2 \text{ x } 3600)$, and corresponding power density (P) of the device was confirmed by the equation: $P = (3600 \text{ x } E) \text{ / } \Delta t$, where C_s represents the gravimetric capacitance, V is the potential window, and Δ_t means the total discharge time.

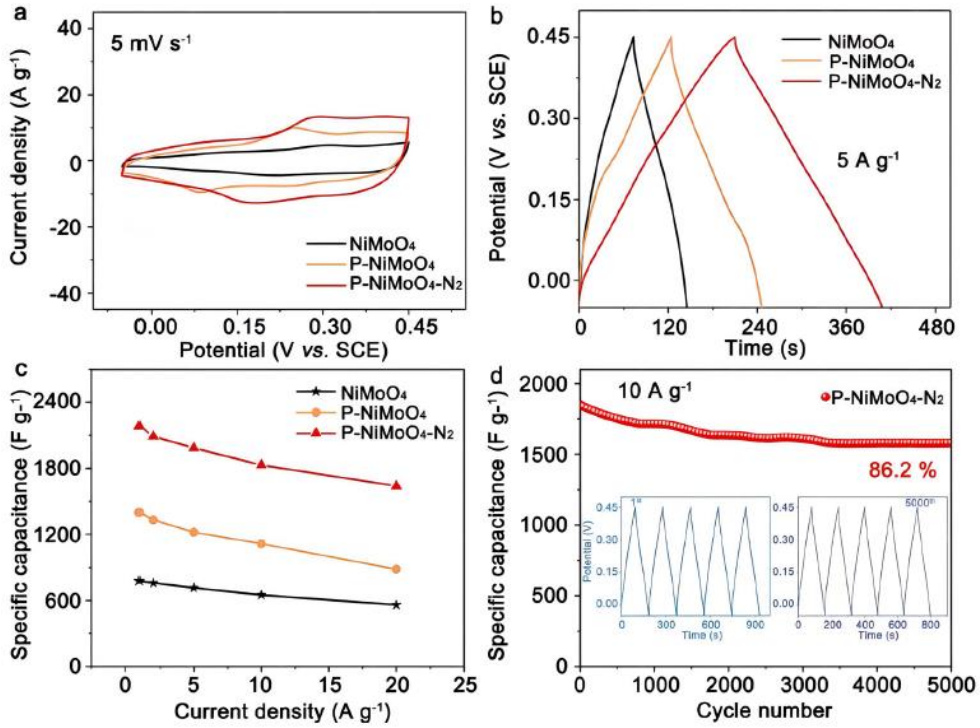

Fig. 3. (a) CV curves at 5 mV s^{-1}, (b) GCD curves in the potential window from — 0.05 to 0.45 V (vs. SCE) at 5 A g^{-1}, (c) specific capacitances at various current densities of $NiMoO_4$, P-$NiMoO_4$ and P-$NiMoO_4$-N_2, and (d) cycling performance of the P-$NiMoO_4$-N_2 at 10 A g^{-1}.

3. Results and discussion

Fig. 1a illustrates the preparation process of P-$NiMoO_4$-N_2 nanosheets arrays. Firstly, the $NiMoO_4$ nanosheets arrays were obtained on Co foam through the hydrothermal method and calcination. Subsequently, the phosphorization and N_2 plasma treatment trigger the P-doping and create defective structures, through which abundant O_v was formed in $NiMoO_4$. **Fig. 1**b presents the XRD images of $NiMoO_4$, P-$NiMoO_4$ and P-$NiMoO_4$-N_2. The characteristic diffraction peaks of all three samples correspond to $NiMoO_4$ (JCPDF No. 86-0361), which suggested that phosphorization and N_2 plasma treatment would not change the crystal structure. **Figs. 1**c and **S1** display the SEM images of P-$NiMoO_4$-N_2, P-$NiMoO_4$ and $NiMoO_4$. They all exhibit the uniform nanosheets arrays on the Co foam. The TEM image of P-$NiMoO_4$-N_2 is illustrated in **Fig. 1**d, where nanosheets show a thickness of ~20 nm. And the HRTEM image (**Fig. 1**e) displays two lattice stripes indicating that different orientations of 0.30 and 0.35 nm correspond to (—311) and (—112) of NiMoO4, respectively. Furthermore, the Mo, Ni, O and P are uniformly distributed on the P-$NiMoO_4$-N_2 nanosheets (**Fig. 1**f-P), thus revealing that the P dopant was well introduced into $NiMoO_4$. As-prepared nanosheets arrays with ultrathin thickness expose more active materials and reduce the 'dead volume', while the P dopant could enhance the surface wettability [**23**].

XPS analyses were further conducted to analyze the elemental composition and chemical valence states of final products. The survey XPS spectra (**Fig. S2**a) depict that all samples include Ni, Mo, and O elements and the extra presence of the P element in P-$NiMoO_4$ and P-$NiMoO_4$-N_2, confirming effective incorporation of P into P-$NiMoO_4$ and P-$NiMoO_4$-N_2. **Fig. 2**a shows the XPS Mo 3d spectra of $NiMoO_4$, P-$NiMoO_4$, and P-$NiMoO_4$-N_2. All three materials exhibit the presence of Mo^{6+} peaks at 235.1 and 232.0 eV [**22**]. After phosphorization, the P-$NiMoO_4$ starts to show a small amount of Mo^{4+} at the peak position of 233.2 and 230.1 eV [**24,25**]. Furthermore, the Mo^{4+} peak intensity of P-$NiMoO_4$-N_2 further increased after the subsequent N_2 plasma treatment, certifying the gradual decrease of Mo valence. The Ni 2p XPS spectra of P-$NiMoO_4$ and P-$NiMoO_4$-N_2 show the characteristic $2p_{3/2}$ and $2p_{1/2}$ doublets with corresponding satellite peaks like those of $NiMoO_4$, ascribed to Ni^{2+} species (**Fig. S2**b). Besides, new deconvoluted peaks centered at 853.2 eV are detected, which can be assigned to $Nis^{+\delta}$ derived from the partial formation of Ni phosphides [**26**]. In the O 1s spectra (**Fig. 2**b), the peak at 532.0 eV was ascribed to P—O bonds, confirming the presence of P-dopant within P-$NiMoO_4$ and P-$NiMoO_4$-N_2 [**27**]. The characteristic peak close to 531.1 eV is responsible to O_v and its content is measured by dividing the peak area of O_v to the total peak areas. $NiMoO_4$ achieves only a small O_v content of 34.3 %. After phosphori-zation, the O_v content of P-$NiMoO_4$ increased to 47.2 %. N_2 plasma treatment further increased the Ov content to 54.5 %. The elevated O_v content might be ascribed to the partial structure transformation from $NiMoO_4$ phase to $Ni_3(PO_4)_2$ phase in the phosphorization process [**22**]. For the P 2p spectrum (**Fig. S2**c), two characteristic peaks with binding energies at 129.4 eV and 133.7 eV are found for P-$NiMoO_4$ and P-$NiMoO_4$-N_2, which correspond to negatively charged $P^{\delta-}$ and phosphates [**28**], while there is no observation of a P signal in $NiMoO_4$. The photoluminescence spectra can also measure the change of O_v content. As shown in **Fig. 2**c, the peak at 530 nm is in accordance with O_v [**29**]. The peak intensity of three samples increases step by step with the phosphorization and N_2 plasma treatment, revealing the gradual increase of Ov contents. Electron paramagnetic resonance (EPR) was also employed to measure O_v. As shown in **Fig. 2**d, a paramagnetic transition at $g = 2.002$ reflects the presence of O_v [**20,30**], which suggested that $NiMoO_4$, P-$NiMoO_4$, and P-$NiMoO_4$-N_2 all have O_v signals and P-$NiMoO_4$-N_2 possesses the highest O_v content, consistent with the results of XPS and PL. The above results clearly suggest that O_v contents follow the order: $NiMoO_4 < P$-$NiMoO_4 < P$-$NiMoO_4$-N_2, and their O_v contents could be increased and modulated through the combination of phosphorization and N_2 plasma treatment. The inset in **Fig. 2**d demonstrates a schematic illustration of the O_v in the crystalline structure. In previous literatures, the increase of O_v in the material could enhance

the conductivity and increase the active sites of the material, thus improving redox reaction kinetics [**31**]. The conductivity of the different materials was calculated by dry-environment CV tests (**Fig. S3**). The electron transfer process affects the voltage-current response, and the slope of the straight line is positively correlated with the conductivity of the material. The P-$NiMoO_4$-N_2 electrode achieves the highest conductivity of 72.3 S cm^{-1}, indicating the increase of intrinsic conductivity derived from the introduction of more O_v.

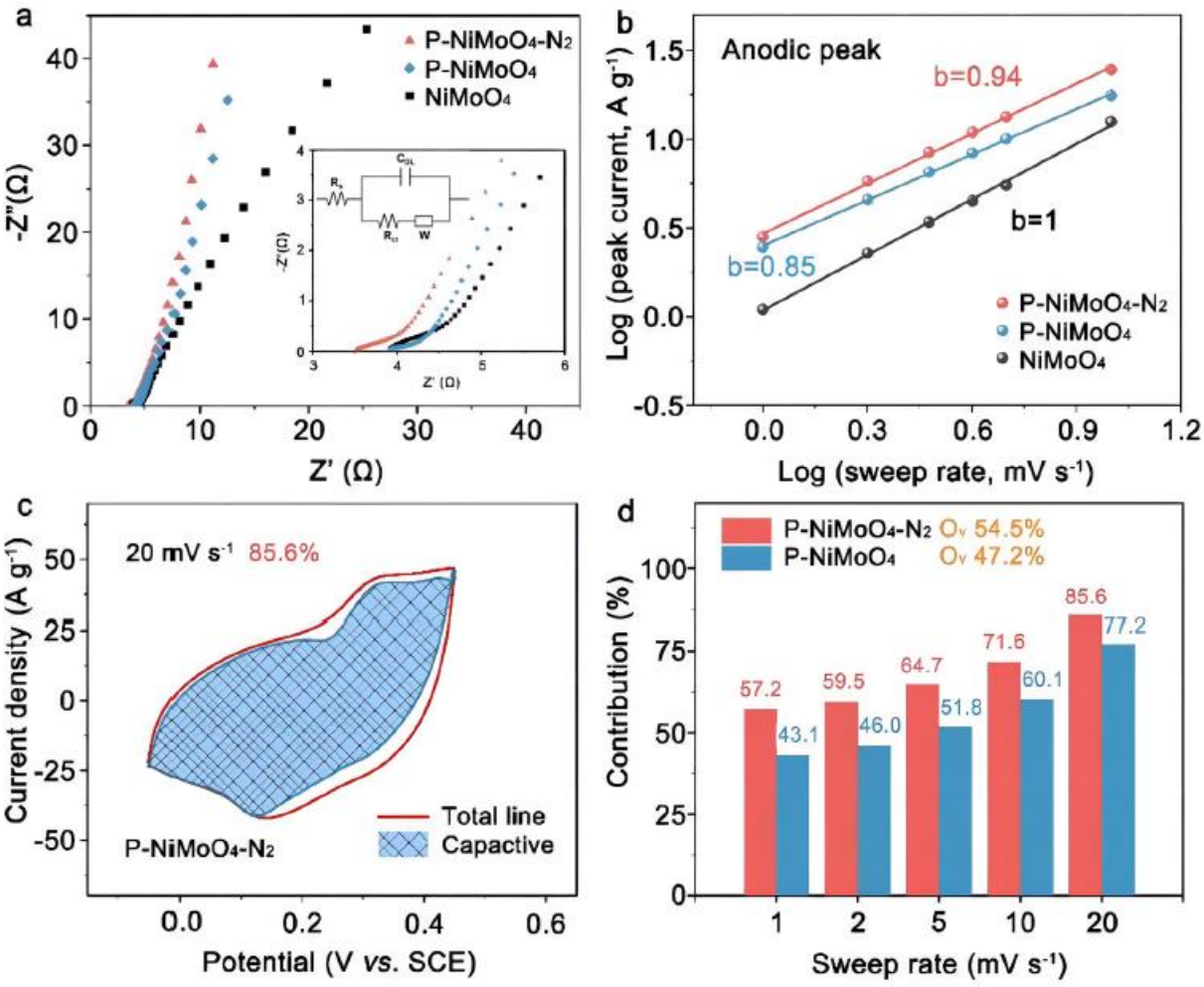

Fig. 4. (a) Nyquist plots, (b) relationships between peak currents and sweep rates for determining b value of the anodic peaks of $NiMoO_4$, P-$NiMoO_4$ and P-$NiMoO_4$-N_2, (c) the capacitive contribution to the total charge storage for P-$NiMoO_4$-N_2 at 20 mV s^{-1}, and (d) normalized contribution proportions of the capacitive at various sweep rates with kinetics and quantitative analysis for P-$NiMoO_4$ and P-$NiMoO_4$-N_2.

The electrochemical performance was measured in a three-electrode system containing a platinum foil counter electrode and a SCE reference electrode. The as-prepared $NiMoO_4$, P-$NiMoO_4$, and P-$NiMoO_4$-N_2 directly served as the free-standing working electrodes. **Fig. 3**a presents the comparison of the CV curves of $NiMnO_4$, P-$NiMoO_4$, and P-$NiMoO_4$-N_2 at a scan rate of 5 mV under an operating potential ranging from —0.05 to 0.45 V. A pair of redox peaks could be observed in the respective CV curve, which can be attributed to the faradaic redox reaction of Ni^{2+}/Ni^{3+} on the electrode surface [**32**]. Notably, the CV curves of P-$NiMoO_4$ and P-$NiMoO_4$-N_2 exhibit larger integral areas than that of $NiMoO_4$, and P-$NiMoO_4$-N_2 shows the largest enclosed CV area among the above three electrodes. The increase in the current density of P-$NiMoO_4$-N_2 could be primarily ascribed to the modulation of P

dopant as well as the improvement of intrinsic conductivity derived from Ov, which synergistically promote the electrochemical activity. GCD tests are conducted at 5 A g^{-1} (**Fig. 3**b). Among three samples, P-$NiMoO_4$-N_2 possesses the longest discharge time (198.5 s), in accordance with CV results. As revealed by the calculation of the specific capacity at several different current densities (**Fig. 3**c), P-$NiMoO_4$-N_2 is found with a high rate capability. It can reach 2180 F g^{-1} at 1 A g^{-1} and remains 1830 F g^{-1} when the current density raises to 10 A g^{-1}. In contrast, the specific capacities of $NiMoO_4$ and P-$NiMoO_4$ at 1 A g^{-1} are much lower (778 and 1400 F g^{-1}) and decrease to 83.5 % and 79.7 % at 10 A g^{-1}, respectively. The electrochemical contribution of bare Co foam was also confirmed via CV and GCD (**Fig. S4**). And it is therefore shown that Co foam itself has negligible current response. It is clear that the capacitance performance of these free-standing electrodes follows the same order as that of Ov contents obtained from XPS, PL, and EPR, thus confirming that increased O_v contents result in enhanced energy storage performances. Subsequently, P-$NiMoO_4$-N_2 with the highest O_v content and superior supercapacitor performances was further investigated for its cycling stability. After 5000 cycling tests (**Fig. 3**d), the capacity retention of P-$NiMoO_4$-N_2 is 86.2 % at 10 A g^{-1}, outperforming those of $NiMoO_4$ (81.7 %) and P-$NiMoO_4$ (76.3 %) (**Fig. S5**). The last 5 charge and discharge curves still maintain good symmetry, demonstrating that the Ov-enriched P-$NiMoO_4$-N_2 is a robust electrode for supercapacitors. Furthermore, for the purpose of practical application, the long-term cycling performance of P-$NiMoO_4$-N_2 was further evaluated for up to 1.000 cycles at a high current density of 20 A g^{-1} (**Fig. S6**). Impressively, 79.7 % of the specific capacitance can be maintained after 11.000cycles. **Fig. S7** shows the SEM image of P-$NiMoO_4$-N_2 after the long-term cycling stability test, which reveals the well-maintained nanosheet feature without structural deformation. The O 1s XPS spectrum of P-$NiMoO_4$-N_2 after the stability test demonstrates that the Ov content (52.1 %) is almost unchanged (**Fig. S8**), indicating an excellent O_v stability of P-$NiMoO_4$-N_2.

The enhanced electrochemical performance of P-$NiMoO_4$-N_2 is further verified by electrochemical impedance spectroscopy (EIS) tests (**Fig. 4**a). It is noteworthy that the series resistance (R_s) confirmed from the intersection of the semicircle with the real axis of $NiMoO_4$, P-$NiMoO_4$, and P-$NiMo_4$-N_2 is 3.91, 3.89 and 3.51 Ω. And charge-transfer resistance (R_{ct}) obtained from the diameter of the semicircle of $NiMoO_4$, P-$NiMoO_4$, and P-$NiMoO_4$-N_2 is 1.17, 0.68, and 0.65 Ω, respectively. The P-$NiMoO_4$-N_2 with the smallest Rs and R_{ct} has the best conductivity, consistent with the result based on the dry-environment CV tests. Moreover, P-$NiMoO_4$-N_2 shows the largest slope in the Nyquist plots, indicating its low charge transfer resistance. These results suggest that the high O_v concentration can enhance the conductivity and provide more active sites for charger-transfer reaction. The CV curves are also adopted to analyze the electrochemical kinetics. **Fig. S9** displays CV curves of P-$NiMoO_4$-N_2, P-$NiMoO_4$, and $NiMoO_4$ at different scan rates from 1 to 5 mV s^{-1}. Typically, the peak anode current (i) obeys a power-law relationship of scan rate (v): i = aV1, where the b value of 0.5 or 1 implies that the kinetics of the electrode is diffusion-controlled or capacitance-controlled processes [**33-35**]. **Figs. 4**b and **S10** show that the b-value of oxidation peaks of P-$NiMoO_4$-N_2 was fitted to be 0.94, closer to 1 than that of P-$NiMoO_4$. The fitted results of the reduction peak are consistent with these of the oxidation peak. Those result indicates that P-$NiMoO_4$-N_2 manifests significant capacitance-controlled processes, guaranteeing faster reaction kinetics and better rate performances. The percentage of capacitive contribution is further quantified and calculated based on the equation: $i = k_4 v + k_2 v^{\frac{1}{2}}$, where the kyv or $k_2 v_2$ represent the capacitive-controlled or diffusion-controlled current. The ratio of $k_1 v$ to i indicates the capacitive contribution [**36,37**]. **Figs. 4**c and **S11** reveal that the capacitive contribution of P-$NiMoO_4$-N_2 (85.6 %) is higher than that of P-$NiMoO_4$ (77.2 %) at a sweep rate of 20 mV s^{-1}. **Fig. 4**d further collects the capacitive contribution of P-$NiMoO_4$-N_2 and P-$NiMoO_4$ at different sweep speeds, which clearly shows P-$NiMoO_4$-N_2 always possesses higher capacitive contributions

than that of P-NiMoO$_4$, indicating that the high O_v content is responsible for the excellent rate performance.

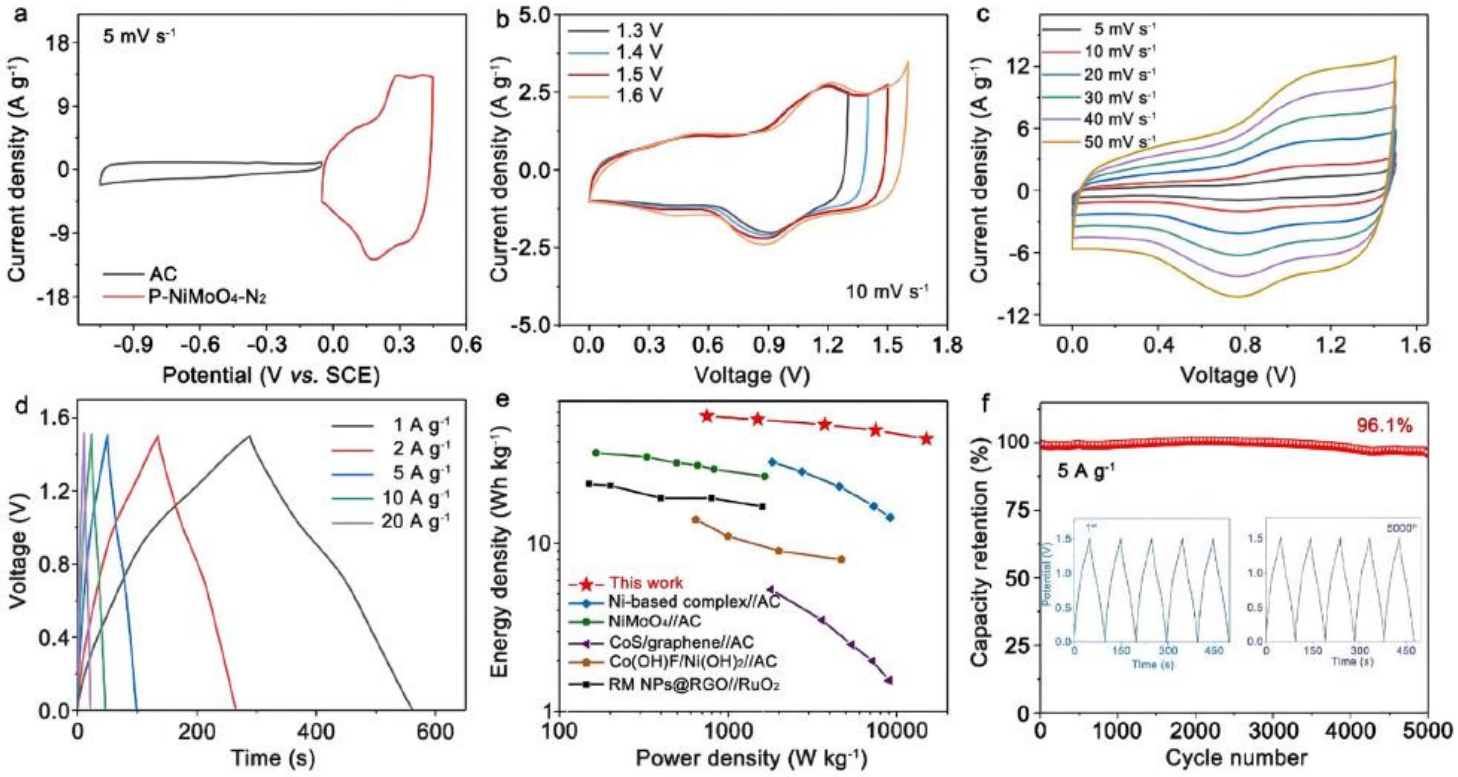

Fig. 5. (a) CV curves of P-NiMoO$_4$-N$_2$ and AC, (b) CV curves with different potential windows, (c) CV curves at different scan rates and (d) GCD curves at various current densities of the P-NiMoO$_4$-N$_2$//AC ASC, (e) Ragone plots for the comparison of P-NiMoO$_4$-N$_2$//AC ASC with literature reports, (f) cycling stability test at 5 A g^{-1} (inset shows GCD curves in the first and the last 5 cycles).

The superior capacitive performances of P-NiMoO$_4$-N$_2$ might be attributed to following three points: (1) abundant O_v created by the phosphorization and N2 plasma treatment acts as extra active sites and effectively improves the intrinsic properties of NiMoO$_4$; (2) the simultaneous incorporation of P dopants enhances the surface wettability; (3) the morphology of nanosheets arrays and their ultrathin thickness are of benefit to the electrolyte mass transfer and avoid 'dead volume'. To further investigate the P-NiMoO$_4$-N$_2$ electrode for practical application, a button-type asymmetric supercapacitor (ASC) was assembled using activated carbon (AC) and P-NiMoO$_4$-N$_2$. **Fig. 5**a shows CV curves of AC and P-NiMoO$_4$-N$_2$ at 5 mV s^{-1}, through which the voltage window of the ASC device can be roughly determined to be 1.5 V without obvious polarization curves (**Fig. 5**b). The CV curves at different sweep rates in 0 to 1.5 V are exhibited in **Fig. 5**c. Notably, a pair of redox peaks could still be clearly observed at high sweep rates, indicating the contribution of pseudocapacitance exists at all scan rates. The GCD curves for different current densities (**Fig. 5**d) also exhibit the little nonlinearity at high current densities, which is congruent with CV results. Moreover, all the charge/discharge curves possess good symmetry, suggesting the high reversibility of the as-prepared button ASC device. The calculated specific capacitance of button ASC device as a function of the discharge current density is plotted in **Fig. S12**. The specific capacitance of ASC device can reach a maximum of 181.8 F g^{-1} at a current density of 1 A g^{-1}. More importantly, ASC reveals excellent rate capability with 73.2 % of capacitance retention even at a current density as high as 20 A g^{-1}. **Fig. 5**e shows the energy density (E) and power density (P) of

ASC calculated from the discharge curves. An energy density reaching 56.8 Wh kg^{-1} can be achieved at a power density of 750 W kg^{-1}. Impressively, the energy density maintains 41.6 Wh kg^{-1} even at high power density of 15,000 W kg^{-1}, demonstrating that this ASC is advantageous over many previously reported materials such as Ni-based complex//AC [**38**], $NiMoO_4$//AC [**39**], CoS/graphene//AC [**40**], $Co(OH)F/Ni(OH)_2$// AC [**41**], and RM NPs@ RGO//RuO_2 [**42**]. In terms of cycling performance, P-NiMoO4-N_2//AC achieves the long-term cycling stability, which retains ~96.1 % of its initial capacitance after 5000 cycles at 5 A g^{-1} (**Fig. 5**f).

4. Conclusions

In summary, the O_v enriched P-$NiMoO_4$-N_2 nanosheet arrays were constructed by two-step phosphorization and N_2 plasma treatment. The surface chemical-state characterization shows the O_v was formed by P-doping during gas-phase phosphorization. Subsequently, N_2 plasma treatment creates abundant defective structure, further increasing the O_v content. The combination strategy of phosphorization and N_2 plasma treatment successfully tune the O_v content in $NiMoO_4$, and the optimized P-$NiMoO_4$-N_2 possesses the highest O_v content, as proved by XPS spectra, PL spectra and EPR spectra. Electrochemical measurements suggest that the high O_v content in the P-$NiMoO_4$-N_2 results in the increase of electrochemical active sites and intrinsic conductivity, which are beneficial for the electrochemical performance. Consequently, P-$NiMoO_4$-N_2 electrode reaches a high capacity of 2180 F g^{-1} at 1 A g^{-1} and maintains 83.9 % at 10 A g^{-1} with an excellent cycling stability. ASC device is assembled by using AC negative electrode. The fabricated device shows the high energy density as high as 56.8 Wh kg^{-1} at 0.75 kW kg^{-1} and remains 41.6 Wh kg^{-1} at 15 kW kg^{-1}. It also exhibits outstanding cycling stability with capacity retention of 96.1 % after 5000 cycles. This work provides an efficient way to introduce and modulate a considerable number of O_v in oxide electrode materials for excellent supercapacitors.

References

[1] L. Wan, D. Chen, J. Liu, Y. Zhang, J. Chen, M. Xie, C. Du, Construction of FeNiP@ CoNi-layered double hydroxide hybrid nanosheets on carbon cloth for high energy asymmetric supercapacitors, J. Power Sources 465 (2020), 228293.

[2] J. Zhao, H. Lai, Z. Lyu, Y. Jiang, K. Xie, X. Wang, Q. Wu, L. Yang, Z. Jin, Y. Ma, J. Liu, Z. Hu, Hydrophilic hierarchical nitrogen-doped carbon nanocages for ultrahigh supercapacitive performance, Adv. Mater. 27 (2015) 3541-3545.

[3] Y. Huang, M. Zhu, Y. Huang, Z. Pei, H. Li, Z. Wang, Q. Xue, C. Zhi, Multifunctional energy storage and conversion devices, Adv. Mater. 28 (2016) 8344-8364.

[4] L. Chen, C. Lian, H. Jiang, L. Chen, J. Yan, H. Liu, C. Li, Dual-conductive N, S codoped carbon nanoflowers for high-loading quasi-solid-state supercapacitor, Chem. Eng. Sci. 217 (2020), 115496.

[5] M. Xie, M. Han, J. Chen, Y. Zhang, C. Du, L. Wan, Y. Chen, High-volumetric supercapacitor performance of ordered mesoporous carbon electrodes enabled by the faradaic-active nitrogen doping and decrease of microporosity, ACS Appl. Energy Mater. 4 (2021) 1840-1850.

[6] W. Wei, Z. Chen, Y. Zhang, J. Chen, L. Wan, C. Du, M. Xie, X. Guo, Full-faradaic-active nitrogen species doping enables high-energy-density carbon-based supercapacitor, J. Energy Chem. 48 (2020) 277-284.

[7] Y. Zhang, L. Cheng, L. Zhang, D. Yang, C. Du, L. Wan, J. Chen, M. Xie, Effect of conjugation level on the performance of porphyrin polymer based supercapacitors, J. Energy Storage 34 (2021), 102018.

[8] S. Peng, L. Li, H.B. Wu, S. Madhavi, X.W. Lou, Controlled growth of NiMoO4 nanosheet and nanorod arrays on various conductive substrates as advanced electrodes for asymmetric supercapacitors, Adv. Energy Mater. 5 (2015) 1401172.

[9] M. Xie, S. Duan, Y. Shen, K. Fang, Y. Wang, M. Lin, X. Guo, In-situ-grown Mg(OH)2-derived hybrid a-Ni(OH)2 for highly stable supercapacitor, ACS Energy Lett. 1 (2016) 814-819.

[10] M. Xie, Z. Xu, S. Duan, Z. Tian, Y. Zhang, K. Xiang, M. Lin, X. Guo, W. Ding, Facile growth of homogeneous Ni(OH)2 coating on carbon nanosheets for high-performance asymmetric supercapacitor applications, Nano Res. 11 (2018) 216-224.

[11] M. Xie, M. Zhou, Y. Zhang, C. Du, J. Chen, L. Wan, Freestanding trimetallic Fe-Co-Ni phosphide nanosheet arrays as an advanced electrode for high-performance asymmetric supercapacitors, J. Colloid Interface Sci. 608 (2022) 79-89.

[12] P. Sharma, M.M. Sundaram, T. Watcharatharapong, D. Laird, H. Euchner, R. Ahuja, Zn metal atom doping on the surface plane of one-dimensional NiMoO4 nanorods with improved redox chemistry, ACS Appl. Mater. Inter. 12 (2020) 44815-44829.

[13] D. Guo, Y. Luo, X. Yu, Q. Li, T. Wang, High performance NiMoO4 nanowires supported on carbon cloth as advanced electrodes for symmetric supercapacitors, Nano Energy 8 (2014) 174-182.

[14] N.S. Neeraj, B. Mordina, A.K. Srivastava, K. Mukhopadhyay, N.E. Prasad, Impact of process conditions on the electrochemical performances of NiMoO4 nanorods and activated carbon based asymmetric supercapacitor, Appl. Surf. Sci. 473 (2019) 807-819.

[15] S. Baskar, V.S. Kalimuthu, K.S. Ramakrishnan, D. Meyrick, M. Minakshi, Nano a-NiMoO4 as a new electrode for electrochemical supercapacitors, RSC Adv. 3 (2013) 352-357.

[16] P. Sharma, M. Minakshi, J. Whale, A.J. Fulcrand, G. Garnweitner, Effect of the anionic counterpart: molybdate vs. tungstate in energy storage for pseudocapacitor applications, Nanomaterials 11 (2021) 580.

[17] J. Yuan, D. Yao, L. Jiang, Y. Tao, J. Che, G. He, H. Chen, Mn-doped NiMoO4 mesoporous nanorods/reduced graphene oxide composite for high-performance all-solid-state supercapacitor, ACS Appl. Energy Mater. 3 (2020) 1794-1803.

[18] Z. Lv, Y. Luo, Y. Tang, J. Wei, Z. Zhu, X. Zhou, W. Li, Y. Zeng, W. Zhang, Y. Zhang, D. Qi, S. Pan, X.J. Loh, X. Chen, Editable supercapacitors with customizable stretchability based on mechanically strengthened ultralong MnO2 nanowire composite, Adv. Mater. 30 (2018) 1704531.

[19] H. Zhang, J. Wang, Q. Cheng, P. Saha, H. Jiang, Highly surface electron-deficient Co9S8 nanoarrays for enhanced oxygen evolution, GreenEnergy Environ. 5 (2020) 492-498.

[20] Q. Xu, Y. Liu, H. Jiang, Y. Hu, H. Liu, C. Li, Unsaturated sulfur edge engineering of strongly coupled MoS2 nanosheet-carbon macroporous hybrid catalyst for enhanced hydrogen generation, Adv. Energy Mater. 9 (2019) 1802553.

[21] S. Ghosh, S. Barg, S.M. Jeong, K. Ostrikov, Heteroatom-doped and oxygen-functionalized nanocarbons for high-performance supercapacitors, Adv. Energy Mater. 10 (2020) 2001239.

[22] F. Wang, K. Ma, W. Tian, J. Dong, H. Han, H. Wang, K. Deng, H. Yue, Y.X. Zhang, W. Jiang, P-doped NiMoO4 parallel arrays anchored on cobalt carbonate hydroxide with oxygen vacancies and mass transfer channels for supercapacitors and oxygen evolution, J. Mater. Chem. A 7 (2019) 19589-19596.

[23] Y. Li, C. Zhao, Enhancing water oxidation catalysis on a synergistic phosphorylated NiFe hydroxide by adjusting catalyst wettability, ACS Catal. 7 (2017) 2535-2541.

[24] L. Chen, H. Jiang, H. Jiang, H. Zhang, S. Guo, Y. Hu, C. Li, Mo-based ultrasmall nanoparticles on hierarchical carbon nanosheets for superior lithium ion storage and hydrogen generation catalysis, Adv. Energy Mater. 7 (2017) 1602782.

[25] L. Bai, C. Wu, G. Lai, Y. Zhu, L. Dong, Z. Zhang, Facile synthesis of C and N codoped MoO2 fibers and their microwave absorption performance, Mater. Lett. 228 (2018) 203-206.

[26] K. Calvinho, A. Laursen, K. Yap, T. Goetjen, S. Hwang, N. Murali, B. Mejia-Sosa, A. Lubarski, K. Teeluck, E. Hall, E. Garfunkel, M. Greenblatt, G. Dismukes, Selective CO2 reduction to C3 and C4 oxyhydrocarbons on nickel phosphides at overpotentials as low as 10 mV, Energy Environ. Sci. 11 (2018) 2550.

[27] Q. Xu, H. Jiang, H. Zhang, H. Jiang, C. Li, Phosphorus-driven mesoporous Co3O4 nanosheets with tunable oxygen vacancies for the enhanced oxygen evolution reaction, Electrochim. Acta 259 (2018) 962-967.

[28] S. Liu, Y. Yin, Y. Shen, K.S. Hui, Y.T. Chun, J.M. Kim, K.N. Hui, L. Zhang, S.C. Jun, Phosphorus regulated cobalt oxide@nitrogen-doped carbon nanowires for flexible quasi-solid-state supercapacitors, Small 16 (2020) 1906458.

[29] J. Zhang, H. Zhang, M. Liu, Q. Xu, H. Jiang, C. Li, Cobalt-stabilized oxygen vacancy of V2O5 nanosheet arrays with delocalized valence electron for alkaline water splitting, Chem. Eng. Sci. 227 (2020), 115915.

[30] S. Yang, Y. Liu, Y. Hao, X. Yang, W.A. Goddard III, X.L. Zhang, B. Cao, Oxygen-vacancy abundant ultrafine Co3O4/graphene composites for high-rate supercapacitor electrodes, Adv. Sci. 5 (2018) 1700659.

[31] C. Qing, C. Yang, M. Chen, W. Li, S. Wang, Y. Tang, Design of oxygen-deficient NiMoO4 nanoflake and nanorod arrays with enhanced supercapacitive performance, Chem. Eng. J. 354 (2018) 182-190.

[32] Q. Xu, H. Jiang, X. Duan, Z. Jiang, Y. Hu, S.W. Boettcher, W. Zhang, S. Guo, C. Li, Fluorination-enabled reconstruction of NiFe electrocatalysts for efficient water oxidation, Nano Lett. 21 (2021) 492-499.

[33] K. Ma, H. Jiang, Y. Hu, C. Li, 2D nanospace confined synthesis of pseudocapacitance-dominated MoS2-in-Ti3C2 superstructure for ultrafast and stable Li/Na-ion batteries, Adv. Funct. Mater. 28 (2018) 1804306.

[34] D.K. Denis, X. Sun, J. Zhang, Y. Wang, L. Hou, J. Li, C. Yuan, Solid solution engineering of Co-Ni-based ternary molybdate nanorods toward hybrid supercapacitors and lithium-ion batteries as high-performance electrodes, ACS Appl. Energy Mater. 3 (2020) 3955-3965.

[35] S. Chen, H. Jiang, Q. Cheng, G. Wang, S. Petr, C. Li, Amorphous vanadium oxides with metallic character for asymmetric supercapacitors, Chem. Eng. J. 403 (2021), 126380.

[36] K. Wei, Y. Zhao, K. Chen, K. Sun, T. Wu, Z. Dong, Y. Cui, C. Zeng, C. Li, Low-overpotential LiF splitting in lithiated fluoride conversion cathode catalyzed by spinel oxide, Adv. Funct. Mater. 31 (2021) 2009133.

[37] L. Hou, T. Xu, R. Liu, H. Yuan, D. Kong, W. Shen, J. Zang, X. Li, Y. Wang, Investigation the sodium storage kinetics of H1.07Ti1.73O4@rGO composites for high rate and long cycle performance, J. Am. Ceram. Soc. 104 (2021) 1526-1538.

[38] L. Song, Y. Han, F. Guo, Y. Jiao, Y. Li, Y. Liu, F. Gao, Mesoporous nickel-based zeolite capsule complex with Fe3O4 as electrode for advanced supercapacitor, J. Nnaomater. 2018 (2018) 9813203.

[39] M.-C. Liu, L. Kang, L.-B. Kong, C. Lu, X.-J. Ma, X.-M. Li, Y.-C. Luo, Facile synthesis of NiMoO4xH2O nanorods as a positive electrode material for supercapacitors, RSC Adv. 3 (2013) 6472-6478.

[40] K. Subramani, N. Sudhan, R. Divya, M. Sathish, All-solid-state asymmetric supercapacitors based on cobalt hexacyanoferrate-derived CoS and activated carbon, RSC Adv. 7 (2017) 6648-6659.

[41] X. Li, R. Ding, W. Shi, Q. Xu, D. Ying, Y. Huang, E. Liu, Hierarchical porous Co(OH) F/Ni(OH)2: a new hybrid for supercapacitors, Electrochim. Acta 265 (2018) 455-473.

[42] K. Annamalai, X. Zheng, J. Gao, T. Chen, Y. Tao, Nanoporous ruthenium and manganese oxide nanoparticles/reduced graphene oxide for high-energy symmetric supercapacitors, Carbon 144 (2019) 185-192.